Chemistry Europe
European Chemical
Societies Publishing

Special Collection

Electrochemical Utilization of Iron IV in the $Li_{1.3}Fe_{0.4}Nb_{0.3}O_2$ Disordered Rocksalt Cathode

Zachary Lebens-Higgins,[a] Hyeseung Chung,[b] Israel Temprano,[c] Mateusz Zuba,[a] Jinpeng Wu,[d] Jatinkumar Rana,[a] Carlos Mejia,[b] Michael A. Jones,[c] Le Wang,[e] Clare P. Grey,[c] Yingge Du,[e] Wanli Yang,[d] Ying Shirley Meng,[b] and Louis. F. J. Piper*[a, f]

Interest in alkali-rich oxide cathodes has grown in an effort to identify systems that provide high energy densities through reversible oxygen redox. However, some of the most promising compositions such as those based solely on earth abundant elements, e.g., iron and manganese, suffer from poor capacity retention and large hysteresis. Here, we use the disordered rocksalt cathode, $Li_{1.3}Fe_{0.4}Nb_{0.3}O_2$, as a model system to identify the underlying origin for the poor performance of Li-rich iron-based cathodes. Using elementally specific spectroscopic probes, we find the first charge is primarily accounted for by iron oxidation to $4+$ below 4.25 V and O_2 gas release beyond 4.25 V with no evidence of bulk oxygen redox. Although the $Li_{1.3}Fe_{0.4}Nb_{0.3}O_2$ is not a viable oxygen redox cathode, the iron $3+/4+$ redox couple can be used reversibly during cycling.

Since the 1990's,[1,2] high energy density iron containing oxides have been pursued for Li-ion batteries as a low cost and non-toxic alternative to the current commercial Ni-rich $LiMO_2$-type layered oxide cathodes.[3] A lot of attention was given to $LiFeO_2$ polymorphs,[1,2,4–10] yet many of these systems show poor capacity retention, and a large voltage hysteresis. In addition, the $LiFeO_2$-type cathodes have a lower average discharge voltage (<3 V) than the Ni-based $LiMO_2$ cathodes (3.5–4.0 V), even though the $Fe^{3+/4+}$ and $Ni^{3+/4+}$ redox couples are predicted around a similar potential.[11–13] These performance issues are often attributed to the inability of Fe^{4+} to stabilize within $LiFeO_2$[2,3] resulting in cycling involving the lower voltage $Fe^{2+/3+}$ redox couple instead. Interest in Fe-based cathodes has been reignited by the growth of novel alkali-rich systems with excess capacities beyond the traditional transition metal (TM) redox couples.[14,15] Novel Fe-based systems including Li_5FeO_4,[16–19] Li_4FeSbO_6,[20] and cation-disordered $Li_{1.24}Fe_{0.38}Ti_{0.38}O_2$,[21] $Li_{1.3}Fe_{0.4}Nb_{0.3}O_2$,[15] and related compositions[22,23] have achieved reversible capacities over 200 mAh/g. As with $LiFeO_2$, these systems often display rapid capacity fade[17,22] and $Fe^{2+/3+}$ activation on cycling.[21,22] The overall stability of the alkali-rich Fe-based cathodes and their ability to achieve high energy densities will be dependent on the underlying redox mechanisms. However, there remains uncertainty over the extent to which iron ($Fe^{3+/4+}$) and oxygen ($O^{2-/n-}$) contribute to the capacity of these cathode materials.[15,17,21–23]

Here, we focus on identifying the underlying charge compensation mechanisms for a model $Li_{1.3}Fe_{0.4}Nb_{0.3}O_2$ disordered rocksalt (DRS) system. During the first charge, delithiation is found to arise from a combination of $Fe^{3+/4+}$ and side-reactions, O_2-gas release and CO_2 generation, with no clear contribution from lattice oxygen redox. The extensive O_2-gas release is demonstrated to activate significant bulk $Fe^{2+/3+}$ redox on discharge. While oxygen redox is not readily stabilized in the Fe-based DRS cathode, the $Fe^{3+/4+}$ redox continues to be accessed reversibly beyond the first cycle.

Throughout this study, we focus on $Li_{1.3}Fe_{0.4}Nb_{0.3}O_2$ materials with micron (4 μm) and nano (200 nm) sized particles. The morphology of these two systems is shown in Figure 1. A phase-pure disordered rocksalt structure was obtained using synthesis temperatures of 950 °C and 750 °C for the micro and nano compounds, respectively (Figure S1). Using this synthesis for the nano system, a homogenous distribution of Fe and Nb are achieved based on scanning transmission electron microscopy and energy-dispersive X-ray spectroscopy (STEM-EDS) elemental mapping (Figure S1). An in-depth discussion of the synthesis of these two Fe-based DRS compounds is given in a previous study.[24]

The 1st, 2nd, and 10th cycle electrochemistry data between 1.5–4.8 V is shown in Figure 1 along with the discharge capacity

[a] Dr. Z. Lebens-Higgins, M. Zuba, Dr. J. Rana, Prof. L. F. J. Piper
Materials Science & Engineering
Binghamton University
Binghamton, NY 13902
[b] H. Chung, C. Mejia, Prof. Y. S. Meng
Department of NanoEngineering
University of California San Diego
La Jolla, CA 92093
[c] Dr. I. Temprano, M. A. Jones, Prof. C. P. Grey
Department of Chemistry
University of Cambridge
Cambridge, CB2 1EW, UK
[d] Dr. J. Wu, Dr. W. Yang
Advanced Light Source,
Lawrence Berkeley National Laboratory
Berkeley, CA 94720
[e] Dr. L. Wang, Dr. Y. Du
Physical and Computational Sciences Directorate
Pacific Northwest National Laboratory
Richland, WA 99354
[f] Prof. L. F. J. Piper
WMG
University of Warwick
Coventry, United Kingdom CV4 7AL
E-mail: louis.piper@warwick.ac.uk

Batteries & Supercaps

Communications
doi.org/10.1002/batt.202000318

Chemistry Europe
European Chemical
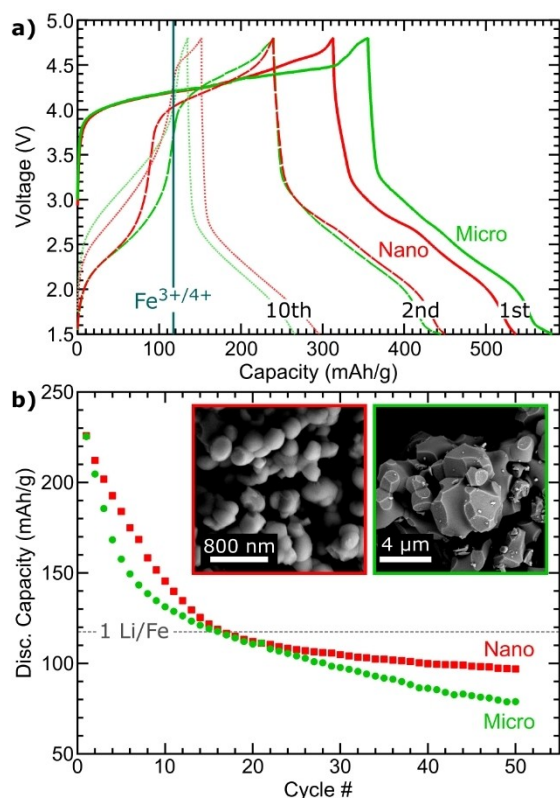Societies Publishing

Figure 1. a) 1st, 2nd and 10th cycle electrochemistry for micro and nano DRS systems and b) discharge capacity during cycling in the voltage range of 1.5–4.8 V at room temperature with a current of 20 mA/g. The inset shows scanning electron microscopy images of the nano and micro systems.

over 50 cycles for the two compounds. First charge/discharge capacities are 356/225 mA h/g and 313/224 mA h/g for the micro and nano DRS compounds, respectively. The theoretical capacity expected from transition metal redox alone is 118 mA h/g based on the $Fe^{3+/4+}$ redox couple (blue line) with the Nb $5+$ (d^0) being redox inactive. Hard X-ray photoelectron spectroscopy measurements of the Nb 3d core region, shown in Figure S2, confirm that niobium is $5+$ and does not participate in the charge compensation. Both systems attain excess charge capacities of over 200 mA h/g, although the excess capacity on discharge drops to around 100 mA h/g. The 2nd and 10th cycles show a drop in the discharge capacity and increased hysteresis during cycling. Looking at the long-term cycling performance, the two systems achieve capacities beyond one lithium per iron site for roughly 16 cycles but do show rapid decay from their initial discharge capacities. Particularly for more electronically insulating cathode systems, such as $LiFePO_4$ and $VOPO_4$, nanosizing has been used to substantially improve the cycling performance.[25,26] A similar improvement might be expected for the $Li_{1.3}Fe_{0.4}Nb_{0.3}O_2$ DRS cathode. However, the micro and nano cathodes show similar fading with the nano having only slightly better long-term performance.

To address the origin of the excess capacity and the rapid capacity fade, we focused on a combination of electronic and structural probes with elemental-specificity to the Fe, Nb and O

environments. Focusing first on the TM environments, Fe and Nb K-edge X-ray absorption near edge structure (XANES) and extended X-ray absorption fine structure (EXAFS) measurements were collected in-situ using a pouch cell setup or ex-situ for coin-cell electrodes. For the micro $Li_{1.3}Fe_{0.4}Nb_{0.3}O_2$, in-situ measurements were collected at select points along the first cycle and then taken at the 2nd charge, 2nd discharge, and 3rd charge. The in-situ cycling profile is shown in Figure S3 along with Nb K-edge XANES spectra. The niobium is found to maintain its $5+$ oxidation state during cycling, although there are reversible changes associated with local structural or chemical changes from (de)lithiation. Select first cycle in-situ Fe K-edge spectra are shown in Figure 2a after charging to 4.2 V (156 mA h/g) and 4.8 V (313 mA h/g) and discharging to 1.5 V (239 mA h/g). Between pristine and 4.2 V, the XANES spectra shows a subtle 0.5 eV edge shift (see inset) along with a corresponding enhancement of the pre-edge peak that likely indicates oxidation of Fe^{3+} to Fe^{4+}. Upon charging to 4.8 V, there is a slight decrease in the edge position. This negative edge shift is not necessarily a reflection of iron reduction given that the pre-edge remained unchanged. For the electrode discharged to 1.5 V, the edge position shifts lower by over 3 eV which is clear evidence for the activation of the $Fe^{2+/3+}$ redox couple based on comparison to an $FeTiO_3$ (Fe^{2+}) reference and suggestive of an almost entirely Fe^{2+} oxidation state in the bulk. Similar line-shape changes were observed for first cycle ex-situ electrodes (Figure S4). The pronounced reduction to Fe^{2+} on discharge is indicative of extensive O_2-gas release occurring on the first charge. This large Fe^{2+} component at the end of discharge is concerning for the overall stability of the DRS cathode as Fe^{2+} is known to dissolve into the electrolyte and contribute to capacity fade in other systems.[27,28]

As the XANES spectra is also dependent on local structural and chemical changes, we conducted fits of the EXAFS region to track the evolution of the Fe—O bond lengths. The Fe—O bond lengths along the first cycle for the in-situ measurements of micro system are given in Figure 2c. Corresponding example fits and fit parameters are given in Figure S5 and Table S2. Along the first charge, the Fe—O bond length decreases between pristine (nominally Fe^{3+})[29] and 4.2 V with around half of the change occurring by 4.1 V (69 mAh/g). Combined with the XANES edge shift, this indicates that $Fe^{3+/4+}$ oxidation occurs during the first part of the charge up to around 4.2 V. Minimal change in the Fe-O bond was observed at higher states of charge indicating the bulk iron maintains its oxidation state. During the discharge process, the Fe—O distance expands slightly by 2.5 V with a more substantial increase by 1.5 V. The average Fe—O distance at 1.5 V is similar to what is obtained for an $FeTiO_3$ reference revealing that the iron in the bulk is almost entirely Fe^{2+} at the end of discharge. During the first discharge, these results indicate bulk $Fe^{4+/3+}$ and $Fe^{3+/2+}$ reduction occurs between 4.8–2.5 V and 2.5–1.5 V, respectively.

Focusing on the evolution of the Fe K-edge during cycling, 1st and 2nd cycle in-situ XANES spectra are shown in Figure 2d. Similar pre-edge and main edge changes are observed during the charge and discharge and the spectra of the 1st and 2nd charge to 4.8 V roughly overlap. Additional comparisons of ex-
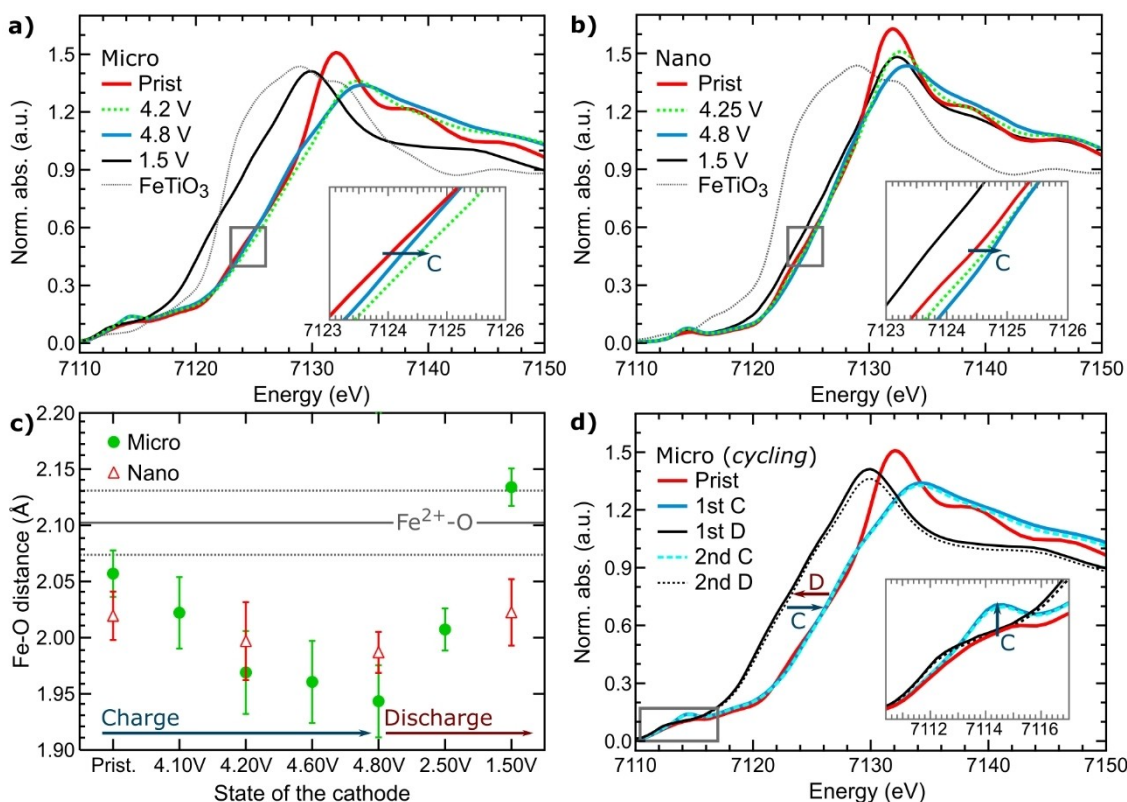
Figure 2. First cycle Fe K-edge XANES spectra of the a) micro (in-situ) and b) nano (ex-situ) systems along with corresponding c) EXAFS fit results for the evolution of the Fe-O bond length. The grey solid line in part c indicates the average Fe^{2+}-O distance based on $FeTiO_3$ reference with the dotted line representing the uncertainty. d) Cycled Fe K-edge spectra for the in-situ measurements of micro Fe DRS. The gray boxed regions in a, b, and d are shown as insets.

situ electrodes taken along the 5th cycle show similar end of charge (4.8 V) spectra as well as continued utilization of the $Fe^{2+/3+}$ redox (Figure S4). Given that the 4.8 V spectra includes signatures of an Fe^{4+} environment, this indicates the continued involvement of multiple iron redox couples ($Fe^{2+/3+}$ and $Fe^{3+/4+}$) on cycling in the bulk. This is further supported by EXAFS fits of the Fe–O distance that show continued contraction beyond the Fe^{3+}-O bond length at the end of the 5th charge (Figure S5). In general, the ex-situ electrodes showed less contraction than the in-situ pouch cell measurements which might point towards some effect that the relaxation time before disassembly and additional storage had on the Fe environment. The two iron redox couples may largely account for the relithiation of the micro Fe DRS cathode as the discharge capacities were below 240 mA h/g (2 el⁻/Fe) for the in-situ and ex-situ cells.

For the nano Fe DRS system, ex-situ Fe K-edge XANES spectra are shown in Figure 2b for electrodes charged to 4.25 V (107 mA h/g), 4.8 V (287 mA h/g), and discharged to 1.5 V (187 mA h/g). The Fe K-edge shows a positive shift upon charging to 4.25 V and 4.8 V. A concurrent shortening of the Fe–O bond distance on charge is observed (Figure 2c). Combined, these changes highlight the utilization of the $Fe^{3+/4+}$ redox couple in the Nano Fe DRS cathode. The XANES spectra for the electrode discharged to 1.5 V shows only a negative 1 eV shift versus the 4.8 V electrode, about a third of

the overall change observed for the micro DRS system. Combined with a shorter endpoint Fe–O distance upon discharge, this indicates less activation of the $Fe^{2+/3+}$ redox couple in the nano system. This is accounted for primarily by the lower discharge capacity of the nano Fe DRS electrode used for XANES.

For the O K-edge measurements, we decided to focus on the nano DRS system as the probing depth of the O K-edge (~ 100 nm) is comparable to the nano particle radius (100 nm), i.e. this probe will be bulk sensitive. This technique will have more contribution from the near-surface region than the Fe K-edge due to an order of magnitude smaller probing depth. O K-edge XAS, a probe of the unoccupied O 2p hybridized states, was collected in surface-sensitive total electron yield (TEY) and bulk-sensitive total fluorescence yield (TFY) modes (Figure 3). From comparison to reference Li_3NbO_4 and $SrFeO_{2.5}$ (Fe^{3+}) in Figure 3a, the spectral features between 529–530 eV and 530.5–532 eV are roughly associated with Fe^{3+} 3d-O 2p and Nb^{5+} 4d-O 2p hybridized states, respectively. An additional peak at 534 eV in the TEY spectra is associated with a carbonate (Li_2CO_3 and $LiHCO_3$) overlayer.[30] The DRS cathodes are more susceptible to ambient exposure resulting in the formation of LiOH, $LiHCO_3$, and Li_2CO_3 on the surface of the $Li_{1.3}Fe_{0.4}Nb_{0.3}O_2$ particles as discussed in our recent study .[24] Features at higher energy (> 535 eV) in the O K-edge are associated with TM s/p-O 2p hybridized states.
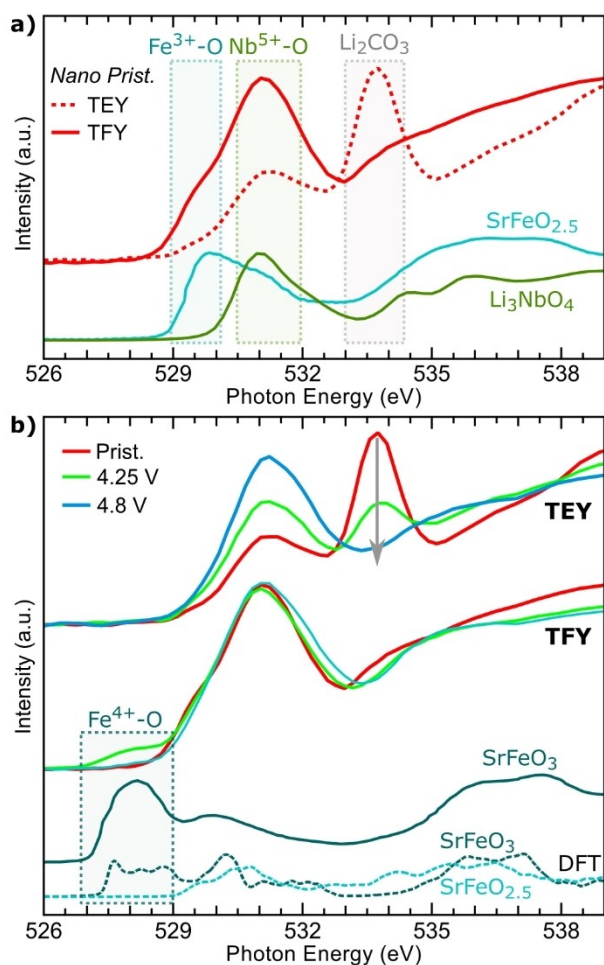
Figure 3. a) Nano DRS Pristine O K-edge spectra compared to $SrFeO_{2.5}$ and Li_3NbO_4 references. b) Evolution of the O K-edge in TEY and TFY modes during the first charge.

Now that we have identified the origin of the spectral features in the O K-edge, we focus on how these features evolve during charge. In the surface-sensitive spectra, the primary effect from pristine to 4.8 V is the breakdown of the Li_2CO_3/$LiHCO_3$ layer, consistent with observations for other oxide cathodes,[31] and no new features are formed. In the bulk-sensitive spectra, a feature emerges at 528 eV at 4.25 V. This feature is at the same excitation energy as observed for our high-quality $SrFeO_3$ reference. In $SrFeO_3$, the iron oxidation is traditionally identified as an Fe^{4+} environment that forms a strong covalent bond with neighboring oxygen atoms[32,33] with this feature being associated with the Fe^{4+}-O hybridized states.[34,35] Additionally, the charged state of the conventional $NaFeO_2$ cathode has a new feature in the O K-edge XAS spectra around the same energy which has also been identified as Fe^{4+}-O hybridization through detailed analysis.[36] Density functional theory (DFT) calculations comparing the $NaFeO_2$ and $SrFeO_{2.5}$ to FeO_2 and $SrFeO_3$ are given in supplementary Figure S6. Both FeO_2 and $SrFeO_3$ show new unoccupied states right above the Fermi level that have Fe 3d and O 2p character. The included $SrFeO_{2.5}$ and $SrFeO_{3.0}$ oxygen partial density of states (PDOS) in Figure 3b capture the emergence of the lower energy peak at

528 eV. Therefore, this pre-edge feature in the Fe DRS system is from the hybridization states of the Fe^{4+}-O which sits several eV lower in energy than the $Fe^{2+/3+}$-O states.[36] The combined experimental and theoretical comparisons point towards the utilization of the $Fe^{3+/4+}$ redox during charging of $Li_{1.3}Nb_{0.4}Fe_{0.3}O_2$ up to 4.25 V, matching with the XANES and EXAFS results. At 4.8 V, this peak is absent indicating the loss of these environments during further charging. Similar loss of the 528 eV pre-edge feature at the end of charge were observed for the Fe-based DRS system in previous studies.[15,22] This contrasts with the Mn-based DRS cathodes that do not show a loss of bulk Mn^{4+}-O peaks during the first charge.[15]

To further confirm the assignment of the 528 eV peak and to look for any evidence of lattice oxygen redox, we performed O K-edge resonant inelastic X-ray scattering (RIXS) measurements. The RIXS technique is the primary method to identify lattice oxidized oxygen (O^{n-}) states with a feature emerging in many alkali-rich cathodes from oxygen redox reactions.[37–41] O K-edge RIXS maps of the pristine material and the 4.25 V electrode are compared to oxygen deficient $SrFeO_{2.5}$ and stoichiometric $SrFeO_{3.0}$ references in Figure 4. In the RIXS map, the energy distribution of the emitted X-ray photons is monitored at each excitation energy used in the X-ray absorption measurements. It has been shown that most TM oxide based oxygen redox systems display a feature in the RIXS maps at an excitation energy of 531 eV and emission energy of 523.7 eV that is a fingerprint of oxygen redox.[37,39–41]

For the pristine material, the broad feature ranging from excitation energies of 529–532 eV is associated with a combination of the Fe^{3+}-O and Nb^{5+}-O hybridized states. Note that this feature is much broader than what is observed for $SrFeO_{2.5}$ or
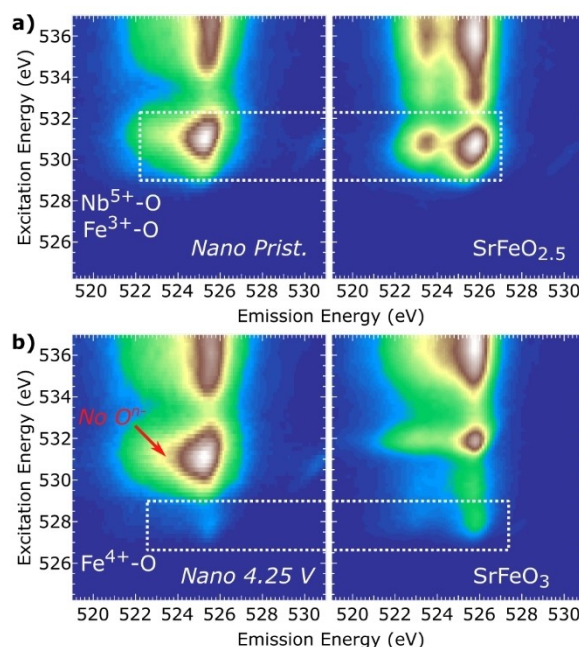

Figure 4. O K-edge RIXS maps for Fe DRS a) pristine sample and b) 4.25 V electrode compared to high-quality $SrFeO_{2.5}$ and $SrFeO_3$ reference spectra. The white boxes highlight the DOS-type features and the red arrow indicates the expected location for O^{n-} states.

Batteries & Supercaps

Communications
doi.org/10.1002/batt.202000318

Chemistry
Europe
European Chemical
Societies Publishing

Li_3NbO_4 (Figure S7), due to the similar location of the Fe^{3+} and Nb^{5+} hybridized states. Upon charging to 4.25 V, a feature emerges at excitation and emission energies of 528 eV and 526 eV, respectively. This feature is at a different location and much broader than the RIXS features observed for peroxides and superoxides[37] and is therefore not associated with the formation of either of these species. Instead, the 528/526 eV feature is more consistent with Fe^{4+} 3d-O 2p hybridized states in the bulk given that it is also found at the exact same location in the $SrFeO_3$ RIXS map. Combined with the positive shift in the XANES spectra and the contraction of the Fe—O bond length between pristine and 4.25 V for the nano Fe DRS cathode, this is conclusive evidence of Fe 4+ formation in the bulk. While previous studies on Li-rich Fe-based cathodes had identified the 528 eV XAS feature as a signature of oxygen redox,[15,16] the RIXS maps reveal that the 528 eV feature is associated with Fe^{4+}.

Beyond utilization of the $Fe^{3+/4+}$ redox couple, the question remains as to the extent of lattice oxygen redox involvement when charging to 4.25 V or beyond. While there is some broadening of the TM-O hybridization feature at 531 eV, this is inconsistent with the formation of O^{n-} states (red arrow in Figure 4b) and likely reflects some structural TM local disordering typically found in alkali-rich cathodes[38,42–44] that can directly affect the TM d-O 2p DOS.[44] More pronounced broadening is observed in the 4.8 V RIXS map (Figure S7) along with the loss of the Fe^{4+}-O states. There is no significant Fe^{4+} to Fe^{3+} reduction observed in the Fe K-edge measurements beyond 4.2 V. Taken together this suggests there is increased heterogeneity above 4.2 V which is discussed in terms of gas evolution below. Additional comparison of individual RIXS slices in Figure S7 to a Li-rich NMC 4.75 V reference electrode shows that there is no evidence that an O^{n-} feature emerges during charge.

As the RIXS method is roughly bulk sensitive for the nano system, the absence of O^{n-} features suggests that the excess first charge capacity results from a different origin than lattice oxygen redox. As such, we undertook online electrochemical mass spectrometry (OEMS) measurements to quantify side-reaction and cathode degradation processes. The electrochemical profile for the nano Fe DRS system in the OEMS setup is shown in Figure 5a, along with the gas evolution data for O_2, CO_2, CO, and H_2. The charge capacity to 4.8 V was 350 mAh/g, similar to what was achieved in coin cell testing (Figure 1a). A rest period at the end of charge under open circuit voltage (OCV) conditions was used to account for all gas evolved during the charge process. The O_2 evolution is found to onset around 4.13 V with a substantial increase in the rate occurring beyond 4.2 V. We assign the source of the O_2 gas to the removal of oxygen from the Fe DRS lattice. The CO_2 evolution turns on at the start of charge and shows a pronounced increase towards the end of charge, similar to the O_2. The turn on towards the start of charge is likely associated with the breakdown of the initial surface carbonate[45] that was observed in the O K-edge. At higher voltages, a substantial increase in CO_2 and CO evolution is observed roughly concurrent with the onset of the O_2 gas. This is likely ascribed to electrolyte
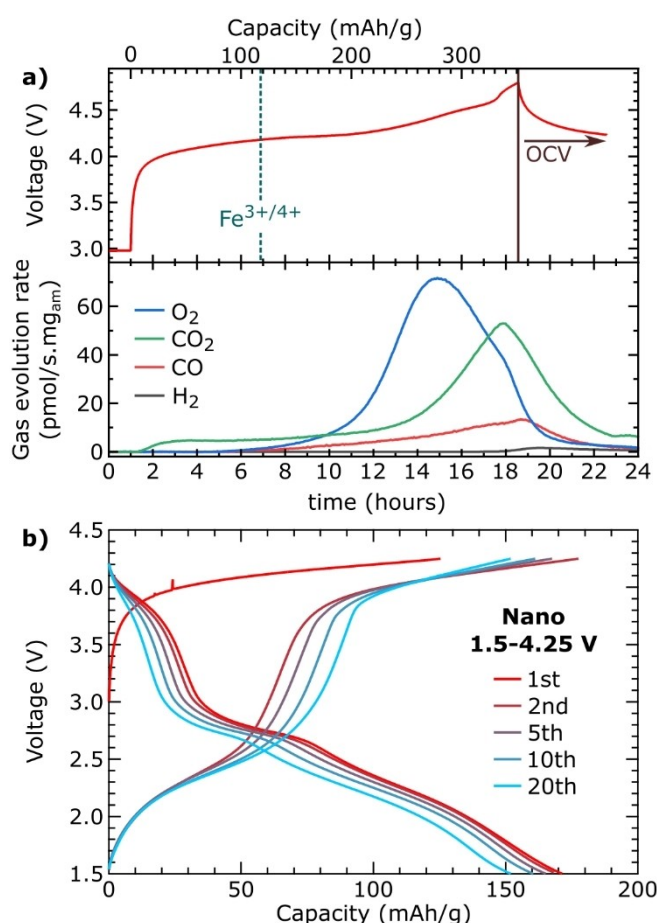

Figure 5. a) OEMS for the first charge for O_2, CO_2, CO and H_2. After the end of charge, the gas evolution continued to be monitored under open-circuit voltage (OCV). b) Electrochemical cycling profile for the nano DRS between restricted voltage window of 1.5–4.25 V.

decomposition reactions that are facilitated by the release of highly reactive oxygen species from the Fe DRS lattice, such as singlet oxygen ($^1O_2$).

During the first charge, the total O_2, CO_2, CO, and H_2 evolved are 1.487 µmol/mg, 1.205 µmol/mg, 0.338 µmol/mg, and 0.002 µmol/mg, respectively. Assuming 4 electrons are transferred as divalent lattice oxygen is removed to form O_2, the total O_2 gas evolved is equivalent to 0.54 Li (or 159 mAh/g). For the total CO_2, CO, and H_2 evolved, an exact determination of their contributions to the capacity is challenging as these species emerge from various electrolyte decomposition reaction pathways[45] as well as the breakdown of Li_2CO_3 from the cathode surface. The breakdown of Li_2CO_3 during charging primarily involves a 2-electron per CO_2 process.[46] Using this as an approximation for the electrolyte contribution from CO_2 as well, the total CO_2 evolved is equivalent to 0.22 Li (or 65 mAh/g). This is an overestimation for the capacity generated from CO_2 evolution, given that CO_2 can form through chemical oxidation of the electrolyte as well.[47] Combining the approximate O_2 and CO_2 contributions with $Fe^{3+/4+}$ redox accounts for around 341 mAh/g or 97% of the total OEMS capacity. Overall, we note that the total quantity of gas evolved for this system

Batteries & Supercaps

Communications
doi.org/10.1002/batt.202000318

Chemistry Europe
European Chemical
Societies Publishing

in OEMS is much higher than observed for other oxide cathodes.[45,48,49] For example, the Mn-based DRS cathode, $Li_{1.3}Mn_{0.4}Nb_{0.3}O_2$, shows a total O_2 and CO_2 of 0.04 μmol/mg and 0.58 μmol/mg, respectively.[48] This highlights just how aggressive the electrolyte and cathode decomposition reactions are for the Fe-based DRS cathode. In general, the Nb-containing DRS compounds have less stability against electrolyte decomposition relative to other Li-rich compounds, e.g. Li-rich NMC, which contributes to higher cell impedance and more rapid capacity loss.[24]

For the Fe-based DRS cathode, the overall capacity is found to originate from $Fe^{3+/4+}$ below 4.25 V and decomposition reactions that induced O_2, CO_2, and CO gas above 4.25 V. While the first few cycles display excess discharge capacities beyond 1 electron

per iron, this is likely accounted for by the combination of the $Fe^{3+/4+}$ (4.8–2.5 V) and $Fe^{2+/3+}$ (2.5–1.5 V) redox couples. The absence of O^{n-} states in $Li_{1.3}Fe_{0.4}Nb_{0.3}O_2$ and the extensive high voltage ($>$4.25 V) degradation is in clear contrast to the reversible oxygen redox in Mn-based cathodes.[15,39,41,48,50] This difference may be largely connected to the higher stability of the Mn^{4+} relative to Fe^{4+} that enables the formation of stable O^{n-} states within Mn-based cathodes. The $Li_{1.3}Fe_{0.4}Nb_{0.3}O_2$ is one of the few examples of an alkali-rich cathode that displays excess capacity but no reversible lattice oxygen redox.[51]

Additional electrochemical cycling between 1.5 and 4.25 V was collected to examine the Fe DRS cathode performance when avoiding high voltage degradation processes. Select cycling profiles for the nano system are shown in Figure 5b and the capacity retention for the nano and micro systems in this voltage window are given in Figure S8. Cycling in the lower voltage window results in more well-defined plateaus on discharge that are maintained during cycling, contrasting the high voltage electrochemistry (Figure 1a). In addition, the nano and micro systems achieve 50th cycle discharge capacities of 138 mAh/g and 149 mAh/g, respectively (Figure S8). It is likely that the $Fe^{3+/4+}$ redox couple is used reversibly due to the similar electrochemical profile on cycling, though there is some contribution from $Fe^{2+/3+}$ given the capacity retention is closer to 150 mAh/g. In this lower voltage window, the $Li_{1.3}Fe_{0.4}Nb_{0.3}O_2$ cathode displays comparable or higher performance than a number of $LiFeO_2$ systems.[3,8,52] This is despite the low iron content and poor kinetics associated with the disordered type materials. This points towards the benefits of stabilizing the $Fe^{3+/4+}$ redox couple through binary oxides as a means towards high energy densities. For example, the $Fe^{3+/4+}$ redox was utilized in the conventional P2-$Na_{2/3}[Fe_{1/2}Mn_{1/2}]O_2$ that demonstrated high energy storage metrics for a sodium cathode.[29]

In summary, we investigated the extent of oxygen and iron redox in the (de)lithiation of the $Li_{1.3}Fe_{0.4}Nb_{0.3}O_2$ cathode. Combining iron and oxygen specific probes, we found clear evidence for the reversible utilization of the $Fe^{3+/4+}$ redox couple on cycling. The origin of the excess capacity in these systems primarily arises from cathode degradation with no reversible bulk lattice oxygen redox. By restricting the upper cutoff voltage to 4.25 V to avoid the cathode degradation regime, the long-term cycling performance can be greatly improved with reversible capacities of ~150 mAh/g involving continued utilization of the $Fe^{3+/4+}$ redox couple.

Conflict of Interest

The authors declare no conflict of interest.

[1] K. Ado, M. Tabuchi, H. Kobayashi, H. Kageyama, O. Nakamura, Y. Inaba, R. Kanno, M. Takagi, Y. Takeda, *J. Electrochem. Soc.* **1997**, *144*, L177.

[2] L. Bordet-Le Guenne, P. Deniard, A. Lecerf, P. Biensan, C. Siret, L. Fournès, R. Brec, *J. Mater. Chem.* **1999**, *9*, 1127–1134.

[3] J. Li, J. Li, J. Luo, L. Wang, X. He, *Int. J. Electrochem. Sci.* **2011**, *6*, 1550–1561.

[4] Y. Koyama, I. Tanaka, Y. S. Kim, S. R. Nishitani, H. Adachi, *Jpn. J. Appl. Phys.,* **1999**, *38*, 4804–4808.

[5] J. Morales, J. Santos-Peña, *Electrochem. Commun.* **2007**, *9*, 2116–2120.

[6] J. Morales, J. Santos-Peña, R. Trócoli, S. Franger, E. Rodríguez-Castellôn, *Electrochim. Acta* **2008**, *53*, 6366–6371.

[7] M. Hirayama, H. Tomita, K. Kubota, R. Kanno, *J. Power Sources* **2011**, *196*, 6809–6814.

[8] A. E. Abdel-Ghany, A. Mauger, H. Groult, K. Zaghib, C. M. Julien, *J. Power Sources* **2012**, *197*, 285–291.

Batteries & Supercaps

Communications
doi.org/10.1002/batt.202000318

Chemistry Europe
European Chemical
Societies Publishing

[9] Y. Hu, H. Zhao, X. Liu, *Materials.* **2018**, *11*, 1–12.

[10] K. Li, H. Chen, F. Shua, K. Chen, D. Xue, *Electrochim. Acta* **2014**, *136*, 10–18.

[11] C. Liu, Z. G. Neale, G. Cao, *Mater. Today* **2015**, *19*, 109–123.

[12] J. Reed, G. Ceder, *Chem. Rev.* **2004**, *104*, 4513–4533.

[13] Y. A. Jeon, S. K. Kim, Y. S. Kim, D. H. Won, B. Il Kim, K. S. No, *J. Electroceram.* **2006**, *17*, 667–671.

[14] G. Assat, J.-M. Tarascon, *Nat. Energy* **2018**, *3*, 373–386.

[15] N. Yabuuchi, M. Nakayama, M. Takeuchi, S. Komaba, Y. Hashimoto, T. Mukai, H. Shiiba, K. Sato, Y. Kobayashi, A. Nakao, M. Yonemura, K. Yamanaka, K. Mitsuhara, T. Ohta, *Nat. Commun.* **2016**, *7*, 13814.

[16] L. Li, E. Lee, J. W. Freeland, T. T. Fister, M. M. Thackeray, M. K. Y. Chan, *J. Phys. Chem. Lett.* **2019**, *10*, 806–812.

[17] C. Zhan, Z. Yao, J. Lu, L. Ma, V. A. Maroni, L. Li, E. Lee, E. E. Alp, T. Wu, J. Wen, Y. Ren, C. Johnson, M. M. Thackeray, M. K. Y. Chan, C. Wolverton, K. Amine, *Nat. Energy* **2017**, *2*, 963–971.

[18] R. Grosjean, S. Delacroix, G. Gouget, P. Beaunier, O. Ersen, D. Ihiawakrim, O. Kurakevych, D. Portehault, *Dalton Trans.* **2017**, *47*, 7634–7639.

[19] A. Hirano, T. Matsumura, M. Ueda, N. Imanishi, Y. Takeda, M. Tabuchi, *Solid State Ionics* **2005**, *176*, 2777–2782.

[20] E. McCalla, A. Abakumov, G. Rousse, M. Reynaud, M. T. Sougrati, B. Budic, A. Mahmoud, R. Dominko, G. Van Tendeloo, R. P. Hermann, J. M. Tarascon, *Chem. Mater.* **2015**, *27*, 1699–1708.

[21] M. Yang, J. Jin, Y. Shen, S. Sun, X. Zhao, X. Shen, *ACS Appl. Mater. Interfaces* **2019**, *11*, 44144–44152.

[22] M. Luo, S. Zheng, J. Wu, K. Zhou, W. Zuo, M. Feng, H. He, R. Liu, J. Zhu, G. Zhao, S. Chen, W. Yang, Z. Peng, Q. Wu, Y. Yang, *J. Mater. Chem. A* **2020**, *8*, 5115–5127.

[23] S. L. Glazier, J. Li, J. Zhou, T. Bond, J. R. Dahn, *Chem. Mater.* **2015**, *27*, 7751–7756.

[24] H. Chung, Z. Lebens-higgins, B. Sayapour, C. Meija, A. Grenier, G. Kamm, Y. Li, R. Huang, L. F. J. Piper, K. Chapman, J.-M. Doux, Y. Shirley Meng, *J. Mater. Chem. A* **2020**.

[25] C. Delmas, M. Maccario, L. Croguennec, F. Le Cras, F. Weill, *Nat. Mater.* **2008**, *7*, 665–671.

[26] C. Siu, I. D. Seymour, S. Britto, H. Zhang, J. Rana, J. Feng, F. O. Omenya, H. Zhou, N. A. Chernova, G. Zhou, C. P. Grey, L. F. J. Piper, M. S. Whittingham, *Chem. Commun.* **2018**, *54*, 7802–7805.

[27] J. Wang, J. Yang, Y. Tang, R. Li, G. Liang, T. K. Sham, X. Sun, *J. Mater. Chem. A* **2013**, *1*, 1579–1586.

[28] K. Amine, J. Liu, I. Belharouak, *Electrochem. Commun.* **2005**, *7*, 669–673.

[29] N. Yabuuchi, M. Kajiyama, J. Iwatate, H. Nishikawa, S. Hitomi, R. Okuyama, R. Usui, Y. Yamada, S. Komaba, *Nat. Mater.* **2012**, *11*, 512–517.

[30] R. Qiao, Y. De Chuang, S. Yan, W. Yang, *PLoS One* **2012**, *7*, 3–8.

[31] Z. W. Lebens-Higgins, S. Sallis, N. V. Faenza, F. Badway, N. Pereira, D. M. Halat, M. Wahila, C. Schlueter, T.-L. Lee, W. Yang, C. P. Grey, G. G. Amatucci, L. F. J. Piper, *Chem. Mater.* **2018**, *30*, 958–969.

[32] P. S. Miedema, F. M. F. De Groot, *J. Electron Spectros. Relat. Phenomena* **2013**, *187*, 32–48.

[33] P. K. Gallagher, J. B. MacChesney, D. N. E. Buchanan, *J. Chem. Phys.* **1964**, *41*, 2429–2434.

[34] V. R. Galakhov, E. Z. Kurmaev, K. Kuepper, M. Neumann, J. A. McLeod, A. Moewes, I. A. Leonidov, V. L. Kozhevnikov, *J. Phys. Chem. C* **2010**, *114*, 5154–5159.

[35] L. Wang, Z. Yang, J. Wu, M. E. Bowden, W. Yang, A. Qiao, Y. Du, *NPJ Mater. Degrad.* **2020**, *4*, 3–8.

[36] S. Roychoudhury, R. Qiao, Z. Zhuo, Q. Li, Y. Lyu, J. Kim, J. Liu, E. Lee, B. J. Polzin, J. Guo, S. Yan, Y. Hu, H. Li, D. Prendergast, W. Yang, *Energy Environ. Mater.* **2020**, *0*, 1–9.

[37] W. E. Gent, I. I. Abate, W. Yang, L. F. Nazar, W. C. Chueh, *Joule* **2020**, *4*, 1369–1397.

[38] W. E. Gent, K. Lim, Y. Liang, Q. Li, T. Barnes, S. Ahn, K. H. Stone, M. McIntire, J. Hong, J. H. Song, Y. Li, A. Mehta, S. Ermon, T. Tyliszczak, D. Kilcoyne, D. Vine, J. Park, S. Doo, M. F. Toney, W. Yang, D. Prendergast, W. C. Chueh, *Nat. Commun.* **2017**, *8*, 2091.

[39] J. Wu, Z. Zhuo, X. Rong, K. Dai, Z. Lebens-Higgins, S. Sallis, F. Pan, L. F. J. Piper, G. Liu, Y. Chuang, Z. Hussain, Q. Li, R. Zeng, Z. Shen, W. Yang, *Sci. Adv.* **2020**, *6*, eaaw3871.

[40] Z. W. Lebens-Higgins, J. Vinckeviciute, J. Wu, N. V. Faenza, Y. Li, S. Sallis, N. Pereira, Y. S. Meng, G. G. Amatucci, A. Van Der Ven, W. Yang, L. F. J. Piper, *J. Phys. Chem. C* **2019**, *123*, 13201–13207.

[41] K. Dai, J. Wu, Z. Zhuo, Q. Li, S. Sallis, J. Mao, G. Ai, C. Sun, Z. Li, W. E. Gent, W. C. Chueh, Y.-D. Chuang, R. Zeng, Z.-X. Shen, F. Pan, S. Yan, L. F. J. Piper, Z. Hussain, G. Liu, W. Yang, *Joule* **2018**, *3*, 518–541.

[42] B. Qiu, B. Zhang, S. Lee, H. Liu, T. A. Wynn, L. Wu, Y. Zhu, W. Wen, C. M. Brown, D. Zhou, Z. Liu, Y. S. Meng, *Cell Rep. Phys. Sci.* **2020**, *1*, 100028.

[43] K. Kleiner, B. Strehle, A. R. Baker, S. J. Day, C. C. Tang, I. Buchberger, F. F. Chesneau, H. A. Gasteiger, M. Piana, *Chem. Mater.* **2018**, *30*, 3656–3667.

[44] J. Rana, J. K. Papp, Z. Lebens-Higgins, M. Zuba, L. A. Kaufman, A. Goel, R. Schmuch, M. Winter, M. S. Whittingham, W. Yang, B. D. McCloskey, L. F. J. Piper, *ACS Energy Lett.* **2020**, *5*, 634–641.

[45] S. E. Renfrew, B. D. McCloskey, *ACS Appl. Mater. Interfaces* **2019**, *2*, 3762–3772.

[46] N. Mahne, S. E. Renfrew, B. D. McCloskey, S. A. Freunberger, *Angew. Chem. Int. Ed.* **2018**, *57*, 5529–5533; *Angew. Chem.* **2018**, *130*, 5627–5631.

[47] B. Rinkel, D. S. Hall, I. Temprano, C. P. Grey, *J. Am. Chem. Soc.* **2020**, *142* 15058–15074.

[48] W. H. Kan, D. Chen, J. K. Papp, A. K. Shukla, A. Huq, C. M. Brown, B. McCloskey, G. Chen, *Chem. Mater.* **2018**, *30*, 1655–1666.

[49] X. Chen, N. Li, E. Kedzie, B. D. Mccloskey, H. Tang, W. Tong, *J. Electrochem. Soc.* **2019**, *166*, A4136–A4140.

[50] R. A. House, U. Maitra, M. A. Pérez-Osorio, J. G. Lozano, L. Jin, J. W. Somerville, L. C. Duda, A. Nag, A. Walters, K. J. Zhou, M. R. Roberts, P. G. Bruce, *Nature* **2020**, *577*, 502–508.

[51] J. Rana, J. K. Papp, Z. Lebens-Higgins, M. Zuba, L. A. Kaufman, A. Goel, R. Schmuch, M. Winter, M. Stanley Whittingham, W. Yang, B. D. McCloskey, L. F. J. Piper, *ACS Energy Lett.* **2020**, *5*, 634–641.

[52] Y. Sakurai, H. Arai, S. Okada, J. I. Yamaki, *J. Power Sources* **1997**, *68*, 711–715.